



Tunable luminescence and energy transfer properties of Bi^{3+} and Mn^{4+} co-doped $\text{Ca}_{14}\text{Al}_{10}\text{Zn}_6\text{O}_{35}$ phosphors for agricultural applications[†]

Li Li,^a Yuexiao Pan,^{*ac} Zhen Chen,^a Shaoming Huang^a and Mingmei Wu^{*b}

A series of Bi^{3+} and Mn^{4+} co-activated $\text{Ca}_{14}\text{Al}_{10}\text{Zn}_6\text{O}_{35}$ (CAZO) phosphors were synthesized using a solid state sintering method. The phase and morphologies of the CAZO based phosphors were confirmed using powder X-ray diffraction (XRD) and scanning electron microscopy (SEM), respectively. A novel phosphor CAZO: Bi^{3+} emits bright blue light under near-ultraviolet (NUV) excitation and its luminescence properties were characterized by diffuse reflectance and photoluminescence spectra. Tunable luminescence from blue to red was observed in Bi^{3+} and Mn^{4+} co-activated CAZO, which is attributed to energy transfer from Bi^{3+} to Mn^{4+} . The energy transfer mechanism has been characterized by the decay times of the Bi^{3+} emission, which changes with the concentration of Mn^{4+} . The energy transfer efficiency from Bi^{3+} to Mn^{4+} increases linearly with increasing the concentration of Mn^{4+} . The as-obtained phosphor has a potential application in agricultural industry because the blue and red lights excited by NUV light emitting diodes (LEDs) are helpful for the improvement of photosynthesis.

Received 31st January 2017
 Accepted 23rd February 2017

DOI: 10.1039/c7ra01285c
rsc.li/rsc-advances

1. Introduction

Artificial lighting in which the wavelengths of the output lighting can be controlled so that they match well with the absorption wavelengths of plant photoreceptors has drawn considerable attention because it can be used to increase crop yield and to tune the plant growth process in phytotrons and greenhouses. Blue light with wavelengths of 400–500 nm and red light with wavelengths of 600–720 nm are indispensable for plant growth because they match the absorption wavelengths of carotenoids and chlorophyll, and improve the photosynthesis of plants.^{1,2} LEDs are attracting much interest due to their energy saving properties and long serving time. Artificial lighting produced by a blue LED and a red LED suffers disadvantages, such as the need for separately driven power supplies, mismatch of the spectral distributions, and color changing with the input power.^{3,4}

Luminescence materials free of rare earth ion doping are currently an active research area for potential applications in

photoelectronic fields due to the lower cost of the raw materials compared to that of rare earth elements. The transition metal ions Bi^{3+} and Mn^{4+} exhibit outstanding optical properties in inorganic solid state crystal lattices, which are attributed to their intrinsic multiple energy levels. The phosphor $\text{LuVO}_4:\text{Bi}^{3+}$ emits efficient yellow emission and is restored to its initial state after eleven rounds of thermal expansion and contraction while the phosphor $\text{ScVO}_4:\text{Bi}^{3+}$ emits strong red-orange light and cannot be restored.⁵ $(\text{Y},\text{Sc})(\text{Nb},\text{V})\text{O}_4:\text{Bi}^{3+}$ exhibits tunable emission spanning from about 450 nm (blue) to 647 nm (orange-red) *via* adjustment of the cations in the host lattice.⁶ The phosphor $\text{ZnWO}_4:\text{Bi}^{3+},\text{Eu}^{3+}$ emits green light with an emission peak at 560 nm and the quenching concentration of Bi^{3+} was greatly increased by energy transfer from Bi^{3+} to Eu^{3+} .⁷ The Bi^{3+} -doped gadolinium tungstate phosphor emits visible radiation from the blue to red regions and an intense near-infrared (NIR) photon centered at 976 nm has been obtained through a quantum-cutting (QC) phenomenon by codoping with Yb^{3+} ions.⁸ Mn^{4+} activated inorganic phosphors, such as fluorides,^{9–11} germanates^{12,13} and aluminates,^{14–17} show potential in the improvement of the color rendition of white LEDs due to their broad and strong absorption in the blue region which matches well with the electroluminescence of blue LED chips. They can produce highly efficient red emission to compensate the red components in the spectrum of the YAG:Ce-GaN type white LED.

Recently, several phosphors based on the host lattice CAZO have been identified as good candidates in various photoelectricity applications with high luminescence efficiency,

^aKey Laboratory of Carbon Materials of Zhejiang Province, College of Chemistry and Materials Engineering, Wenzhou University, Wenzhou 325035, P. R. China. E-mail: xypan8@gmail.com; Fax: +86-577-8837-3017; Tel: +86-577-8837-3017

^bMOE Key Laboratory of Bioinorganic and Synthetic Chemistry, School of Chemistry and Chemical Engineering, Sun Yat-Sen University, Guangzhou 510275, P. R. China. E-mail: ceswmm@mail.sysu.edu.cn; Tel: +86-20-84111823

^cKey Laboratory of Optoelectronic Materials Chemistry and Physics, Chinese Academy of Sciences, Fuzhou, Fujian 350002, China

† Electronic supplementary information (ESI) available. See DOI: [10.1039/c7ra01285c](https://doi.org/10.1039/c7ra01285c)



chemically and physically stable characteristics, ease of synthesis, and low cost of raw materials.^{16–20} Even though the luminescent properties of rare earth ions and Mn⁴⁺ in the host lattice CAZO have been extensively studied, blue emission luminescence from Bi³⁺ in CAZO has not been observed. It is worth investigating the efficient energy transfer between the two transition metal ions Bi³⁺ and Mn⁴⁺ owing to the energy match between the ³P₁ (Bi³⁺) and ²E (Mn⁴⁺) levels.

In this work, we report the observation of strong blue emission in a novel phosphor CAZO:Bi³⁺. Moreover, a phosphor CAZO:Bi³⁺,Mn⁴⁺ has been achieved and its emission color can be easily tuned by controlling the relative intensity ratio of the blue emission from Bi³⁺ and the red emission from Mn⁴⁺. The optimized internal quantum yield (QY) of the phosphor is as high as 89.1%, which is due to the efficient energy transfer from Bi³⁺ to Mn⁴⁺.

2. Experimental

2.1 Synthesis of the phosphors CAZO:Bi³⁺ and CAZO:Bi³⁺,Mn⁴⁺

A series of powder samples were synthesized using a solid state reaction technique at high temperature. The solid state reagents CaCO₃ (A.R.), Al₂O₃ (A.R.), ZnO (A.R.), Bi₂O₃ (A.R.) and MnCO₃ (A.R.) were used as starting materials and weighed according to the stoichiometric compositions of the compounds Ca_{14-x%}Al₁₀Zn₆O₃₅:x% Bi³⁺ ($x = 0.05, 0.1, 0.5, 1, 2, 3, 4$ or 5) and Ca_{13.995}Al_{10-x%}Zn₆O₃₅:0.5% Bi³⁺,x% Mn⁴⁺ ($x = 0.05, 0.1, 0.2, 0.25, 0.3, 0.35, 0.45, 0.5$ or 1). The starting materials were mixed thoroughly by grinding in an agate mortar for 30 min. The powder mixtures were first sintered at 700 °C for 5 h and then sintered at 1150 °C for 5 h in air. After having cooled down to room temperature in the furnace, the samples were ground into powders for further measurement.

2.2 Characterization

The phase formation and crystal structure determination of the products were identified using a Bruker (Karlsruhe, Germany) D8 Advance X-ray powder diffractometer (XRD) with graphite monochromatized Cu K α radiation ($\lambda = 0.15418$ nm). The XRD data were collected in the range of 10–80°. The morphology and structure of the samples were studied using field emission scanning electron microscopy (FE-SEM) on a Nova NanoSEM 200 scanning electron microscope. UV-vis diffuse reflectance spectra were measured using a Shimadzu UV-3600 spectrometer. Photoluminescence (PL) spectra were recorded using a FluoroMax-4 spectrofluorometer (Horiba Jobin Yvon Inc.) with a 150 W xenon lamp with a heating attachment. The internal QY was measured using an integrating sphere coated with barium sulfate.

3. Results and discussion

3.1 Crystal structure and morphologies

The XRD patterns of the as-prepared samples of CAZO, CAZO:0.2% Mn⁴⁺, CAZO:1% Bi³⁺ and CAZO:0.2% Mn⁴⁺,1% Bi³⁺

were obtained to verify the phase purity. As shown in Fig. 1a, all of the peaks of undoped CAZO and the phosphors match well with the standard data of CAZO in the Joint Committee on Powder Diffraction Standards (JCPDS) file No. 50-0426. The sharp crystalline features observed in the XRD profiles indicate that micrometer particles with good crystallinity were obtained using the solid state synthesis method. The introduction of Bi³⁺ and Mn⁴⁺ does not cause significant changes in the crystal structure of the host lattice, which illustrates that Bi³⁺ and Mn⁴⁺ have been effectively built into the host lattice in the form of a solid solution.

Fig. 1b displays a partial structural overview of CAZO and the coordination environment of the cation sites in CAZO. In the crystal lattice of CAZO, four fifths of the positions occupied by Al and Zn are in a tetrahedral coordination, and the one fifth dependent position is in an octahedral coordination. In this structure, Ca²⁺ has three different coordination environments.^{16,19} Two of them are in a six-coordinated octahedron, and the third one is in a seven-coordinated polyhedron. On the basis of the effective ionic radii with different coordination numbers, Bi³⁺ ($r = 0.117$ nm) ions are expected to randomly occupy the six- and seven-coordinated Ca²⁺ ($r = 0.114$ nm; $r = 0.120$ nm) sites, and Mn⁴⁺ ($r = 0.067$ nm) ions are preferentially accommodated at the Al³⁺ ($r = 0.067$ nm) sites in the centers of the octahedron coordinated by the O²⁻ ions in the crystal structure.^{16,19} To keep the electroneutrality of the compound, excess O²⁻ ions may form for charge compensation. Fig. 1c presents typical SEM images of the CAZO:0.5% Bi³⁺, CAZO:0.2% Mn⁴⁺ and CAZO:0.5% Bi³⁺,0.2% Mn⁴⁺ samples; the morphologies of the samples exhibit aggregations and irregularity, and the diameters are observed to range from sub-micrometer to a few micrometers.

3.2 Photoluminescence of the blue phosphor CAZO:Bi³⁺

The light absorption capability of the as-prepared samples of CAZO:Bi³⁺ has been evaluated using the reflectance from BaSO₄ as a reference. The UV-vis diffuse reflectance spectra of CAZO:Bi³⁺ with various concentrations of Bi³⁺ are shown in Fig. 2a. For all of the samples, two absorption bands peaking at 290 and 380 nm in the UV-visible region are observed, which are attributable to the ¹S₀–¹P₁ and ¹S₀–³P₁ transitions of Bi³⁺, respectively. With increasing the concentration of the Bi³⁺ ions, the absorption is intensified and the band edge extends to the longer wavelength, which yields the daylight color of powder samples ranging from white to pale brown.

Fig. 2b shows the emission and excitation spectra of the as-synthesized Bi³⁺ ion singly doped CAZO phosphor. The excitation spectrum of CAZO:Bi³⁺ monitored at 410 nm consists of two bands with a maximum at 346 nm, which matches well with the electroluminescence wavelength of NUV chips for agricultural applications. Although LED chips with wavelengths at about 346 nm are not currently dominant, they are commercially available, so it is significant to develop a phosphor upon this excitation wavelength especially free of rare earth elements. The weak absorption band at 260 nm and the strong one at 346 nm are ascribed to the parity-allowed transitions ¹S₀–¹P₁



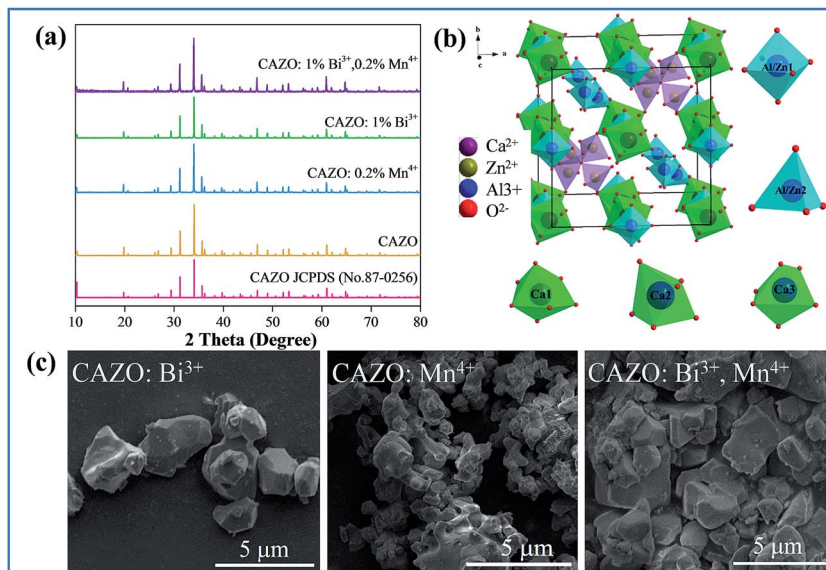


Fig. 1 (a) XRD patterns of the as-prepared phosphors CAZO:0.2% Mn⁴⁺, CAZO:1% Bi³⁺ and CAZO:1% Bi³⁺,0.2% Mn⁴⁺ and the standard data for CAZO (JCPDS No. 87-0256) shown as a reference. (b) Crystal structure of the CAZO unit cell viewed in the *c*-direction and the coordination environment of the cation Ca²⁺ sites in CAZO. (c) The SEM images of CAZO:0.5% Bi³⁺, CAZO:0.2% Mn⁴⁺ and CAZO:0.5% Bi³⁺,0.2% Mn⁴⁺.

and $^1S_0-^3P_1$ of Bi³⁺, respectively.²¹ The emission spectrum of CAZO:Bi³⁺ exhibits an intense and broad band in the region of 400–600 nm peaking at 410 nm with a full width of half-maximum (FWHM) around 86 nm, which is assigned to the $^3P_1-^1S_0$ transition of Bi³⁺ ions.

Fig. 3 shows the emission spectra and color of the samples of CAZO: $x\%$ Bi³⁺ ($x = 0.05, 0.1, 0.5, 1, 2, 3, 4$ or 5) changing with the Bi³⁺ concentration. As shown in Fig. 3a, all of the emission spectra of CAZO:Bi³⁺ demonstrate broadening spectral profiles, and the emission bands of Bi³⁺ give an evident red-shift. We can see from Fig. 3b that the emission bands of Bi³⁺ shift from 396 to 436 nm as the Bi³⁺ concentration increases from 0.05 to 5 mol%. The red shift may result from two reasons: (i) the change of the CAZO crystal field by substitution of Ca²⁺ with Bi³⁺ due to the small difference in the two ionic radii, which results in the increasing of the crystal field strength around Bi³⁺ and the splitting of the 3d energy level of Bi³⁺,^{22–24} (ii) the increase of the energy transfer probability between Bi³⁺ ions which reduces the high-energy portion in the whole emission profile, and then lowers the overall energy as represented by the red shift.²⁵ It can be observed that the emission intensity of the Bi³⁺ ions increases with increasing doping concentration, reaches a maximum at $x = 0.5$, and then decreases sharply when the Bi³⁺ concentration is higher than 0.5 mol% due to concentration quenching. The highest photoluminescence intensity was achieved at $x = 0.5$. The corresponding photographs of the samples with varied concentration of Bi³⁺ ions are shown in Fig. 3c. The daylight color of the samples changes from white to pale brown with an increase of the Bi³⁺ concentration, which is consistent with the results of the UV-vis diffuse reflection spectra. The samples with low Bi³⁺ concentrations ($x = 0.05$ and 0.1) show purple-blue and those with high Bi³⁺ concentrations ($x \geq 0.5$) emit blue light upon excitation by a UV lamp.

3.3 Tunable luminescence of the Bi³⁺ and Mn⁴⁺ co-doped CAZO phosphor *via* energy transfer

Fig. 4a shows the luminescence and UV-vis diffuse reflection spectra of CAZO:Mn⁴⁺. As expected for substitution of Al³⁺ with Mn⁴⁺ in an oxide host CAZO, the d-d transition of Mn⁴⁺ within its 3d³ electron configuration produces red light at about 690 nm. As shown in Fig. 4a, the emission band of CAZO:Mn⁴⁺ with a group of sharp peaks is attributed to transitions between the vibronic levels of 2E and 4A_2 of Mn⁴⁺. The excitation spectra exhibit two typical absorption bands at 314 and 467 nm, which are attributed to the $^4A_2-^4T_1$ and $^4A_2-^4T_2$ transitions of the Mn⁴⁺ ion in the octahedral coordination, respectively. The white powder CAZO:Mn⁴⁺ has a reflectance of about 90% in the visible region and exhibits two absorption bands in the NUV region and blue regions in the diffuse reflection spectra of CAZO:Mn⁴⁺, which is consistent with its excitation spectra.

A strong and broad absorption band of CAZO:Mn⁴⁺ in the blue range overlaps with the emission of CAZO:Bi³⁺, which provides the possibility for energy transfer from Bi³⁺ to Mn⁴⁺ ions in the host lattice CAZO. To confirm the phenomenon of energy transfer from the Bi³⁺ to Mn⁴⁺ ions, a series of Bi³⁺ and Mn⁴⁺ co-doped CAZO samples were prepared. Fig. S1† shows the excitation spectra of the phosphor CAZO:1% Bi³⁺,0.5% Mn⁴⁺ monitored at 417 nm and 712 nm. The band at 346 nm in the excitation spectrum monitored at 417 nm is attributed to the $^1S_0-^3P_1$ transition of Bi³⁺ as observed in the excitation spectrum of Bi³⁺ singly doped CAZO. In the excitation spectrum monitored at 712 nm, the band between 250 and 400 nm is jointly originated from the $^1S_0-^3P_1$ transition of Bi³⁺ and the $^4A_2-^4T_1$ transition of Mn⁴⁺. The strong absorption band in the range of 400–500 nm is attributed to the $^4A_2-^4T_2$ transition of Mn⁴⁺, which is overlapping with the emission of Bi³⁺. Fig. 4b illustrates the emission spectra of the typical samples of



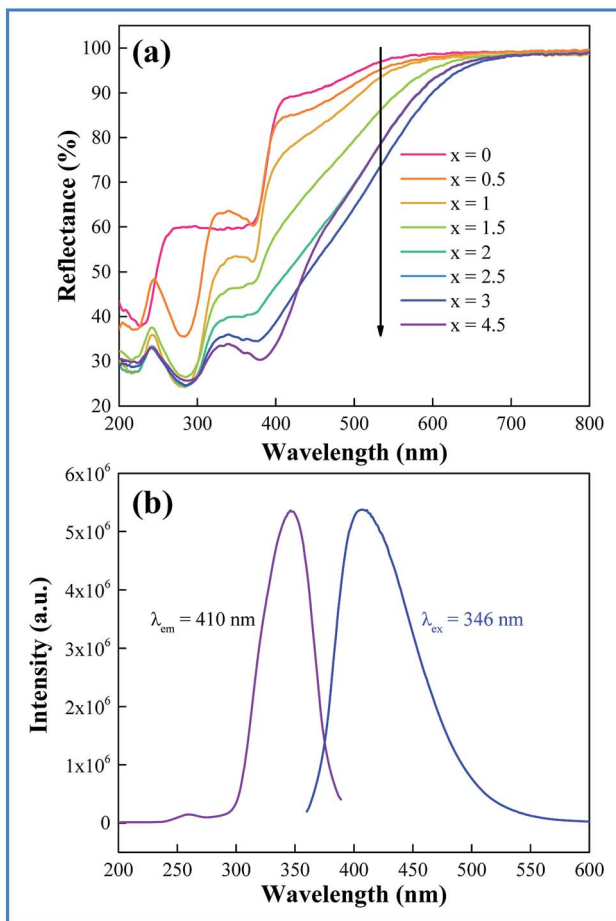
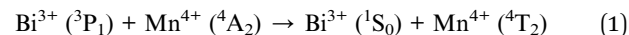


Fig. 2 (a) UV-vis diffuse reflection spectra of the as-synthesized phosphors CAZO:x% Bi³⁺ with different concentrations, x, of Bi³⁺ (x = 0, 0.5, 1, 1.5, 2, 2.5, 3 or 4.5). (b) Excitation ($\lambda_{\text{em}} = 410$ nm) and emission ($\lambda_{\text{ex}} = 346$ nm) spectra of a typical sample of CAZO:1% Bi³⁺.

CAZO:0.5% Bi³⁺,x% Mn⁴⁺ (x = 0.05, 0.1, 0.2, 0.3, 0.35, 0.4 or 0.5) excited at 351 nm. It is found that both blue light from Bi³⁺ and red light from Mn⁴⁺ are produced in all of the Bi³⁺ and Mn⁴⁺ co-doped CAZO samples. The emission band from 400 nm to 550 nm with a maximum at 410 nm is ascribed to the $^3\text{P}_1$ – $^1\text{S}_0$ transition of Bi³⁺ ions while that from 650 nm to 750 nm is ascribed to the ^2E – $^4\text{A}_2$ emission of Mn⁴⁺ ions. Fig. S2† shows that the red emission of CAZO:0.5% Bi³⁺,0.5% Mn⁴⁺ matches well with the absorption of chlorophyll A and the blue emission overlaps with the absorption of both chlorophyll A and chlorophyll B, which indicates the potential application of the phosphor in artificial lighting. Furthermore, as shown in Fig. 4c, the intensity of the blue emission decreases and that of the red emission increases with increasing the Mn⁴⁺ concentration, which is indicative of the occurrence of energy transfer between Bi³⁺–Mn⁴⁺. The red emission intensity arrives at a maximum at x = 0.4 due to concentration quenching. Thanks to the variation of the emission spectra of the CAZO:Bi³⁺,Mn⁴⁺ phosphors with varying Mn⁴⁺ concentration, the emission color can be tuned via changing the Bi³⁺/Mn⁴⁺ ratio.

The schematic energy level diagram for the electronic transitions and the energy transfer process in Bi³⁺ and Mn⁴⁺ co-doped CAZO are shown in Fig. 4d. Under excitation at 351 nm, the Bi³⁺ ions are initially excited from the ground state $^1\text{S}_0$ to the excited state $^3\text{P}_1$. Some of the Bi³⁺ ions return to the ground state $^1\text{S}_0$ through radiative transition and yield blue emission. The other Bi³⁺ ions at the $^3\text{P}_1$ state transfer their energy to the adjacent Mn⁴⁺ ions and promote Mn⁴⁺ ions from the ground state $^4\text{A}_2$ to the excited state $^4\text{T}_2$ as follows:



The Mn⁴⁺ ions in the ${}^4\text{T}_2$ state relax to the ${}^2\text{E}$ level through a non-radiative transition and then produce red emission when they return to the ground state ${}^4\text{A}_2$.

In order to better understand the energy-transfer sensitization mechanism, the luminescence decay times of the 410 nm emission of Bi³⁺ in the CAZO:0.5% Bi³⁺,x% Mn⁴⁺ (x = 0.05–0.5) phosphors have been measured with excitation at 346 nm as shown in Fig. 5. All of the decay curves can be fitted using a single-exponential decay:

$$I_t = I_0 \exp(-t/\tau) \quad (2)$$

where I_0 and I_t are the luminescence intensities at times t_0 and t_1 , respectively; τ denotes the decay time of luminescence from the corresponding samples, which could be easily calculated by fitting the decay curves. The decay times were determined to be 9.31, 8.98, 8.85, 8.81, 8.42, 8.31, and 7.57 μs for the samples of CAZO:0.5% Bi³⁺,x% Mn⁴⁺ with x = 0.1, 0.15, 0.2, 0.3, 0.35, 0.4, and 1.0, respectively.

The lifetime of Bi³⁺ decreases from 9.31 to 7.57 μs when the Mn⁴⁺ content is increased from 0.10 to 1.0 mol%, which is indicative of the increasing non-radiative energy transfer rate. The non-radiative energy transfer of Bi³⁺ ions changing with Mn⁴⁺ content may be mainly ascribed to the energy transfer from Bi³⁺ to Mn⁴⁺. Generally, in oxide phosphors, the exchange interaction or multipole–multipole interaction comes into effect only when the distance between the sensitizer and activator is shorter than 5.0 \AA .²⁶ The critical distance among the Bi³⁺ and Mn⁴⁺ ions can be calculated using the following equation:²⁷

$$R_c \approx 2[3V/4\pi x_c N]^{1/3} \quad (3)$$

where V is the volume of the unit cell, N is the number of cations in the unit cell, and x_c is the sum content of Bi³⁺ and Mn⁴⁺ ions. For the CAZO host, $V = 3286.68 \text{ \AA}^3$ and $N = 4$. Here, for the case of $x_c = 0.01$, R_c is found to be 31 \AA , which is greater than 5 \AA . Thus, the multipolar interaction is dominantly responsible for the energy transfer from Bi³⁺ to Mn⁴⁺ in the CAZO phosphors. The energy transfer efficiency (η_T) from Bi³⁺ to Mn⁴⁺ could be estimated by the following:^{27–29}

$$\eta_T = 1 - \frac{\tau_0}{\tau_s} \quad (4)$$

where τ_{s0} and τ_s are the corresponding intrinsic decay lifetimes of the sensitizer (Bi³⁺) in the absence and presence of the

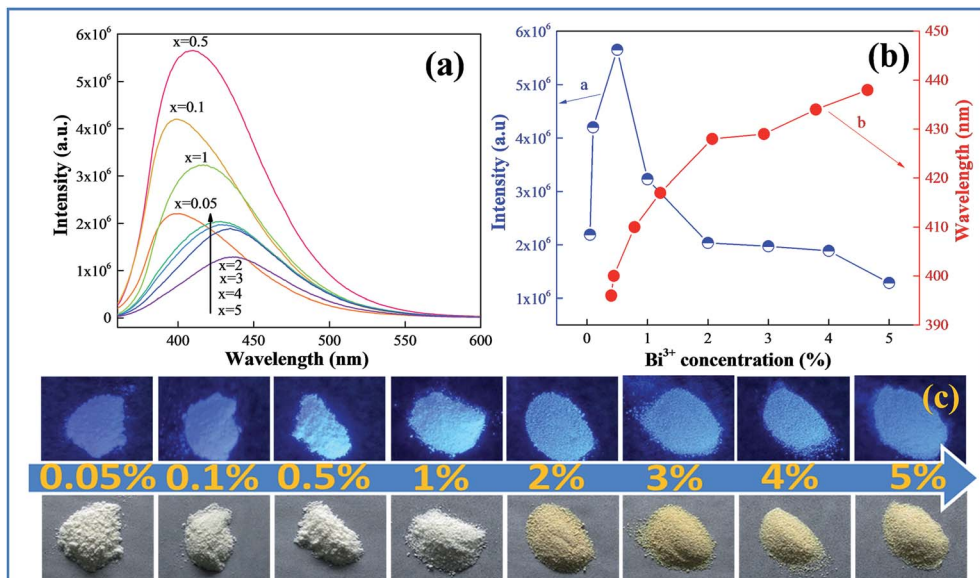


Fig. 3 (a) Emission spectra ($\lambda_{\text{ex}} = 346 \text{ nm}$) of typical samples of CAZO:x% Bi³⁺ ($x = 0.05, 0.1, 0.5, 1, 2, 3, 4$ or 5). (b) Dependence of the emission intensities on the Bi³⁺ concentrations (blue line), and the variation in the red shift of Bi³⁺ emission with increasing concentration of Bi³⁺ (red line). (c) Photographs of the CAZO:x% Bi³⁺ phosphors with changing the concentration of Bi³⁺ under 365 nm UV (upper line) and visible light (lower line).

acceptor of Mn⁴⁺, respectively. The η_T from Bi³⁺ to Mn⁴⁺ calculated on the basis of eqn (4) shows that the energy transfer efficiency was found to increase gradually with increasing the

Mn⁴⁺ content when the concentration of Bi³⁺ is fixed, as illustrated in Fig. 5b. The maximum value of η_T can reach about 23.7% in the as-prepared samples.

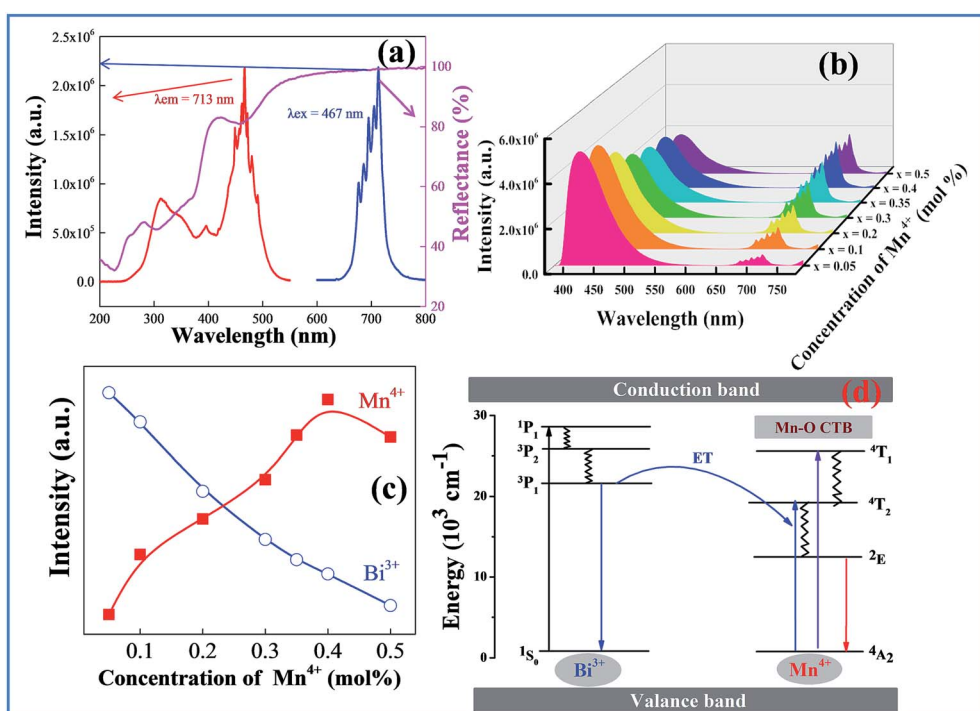


Fig. 4 (a) Emission ($\lambda_{\text{ex}} = 467 \text{ nm}$) and excitation ($\lambda_{\text{em}} = 713 \text{ nm}$) spectra, and UV-vis diffuse reflection spectra of a typical sample of CAZO:Mn⁴⁺. (b) Emission spectra ($\lambda_{\text{ex}} = 351 \text{ nm}$) of samples of CAZO:0.5% Bi³⁺,x% Mn⁴⁺ ($x = 0.05, 0.1, 0.2, 0.3, 0.35, 0.4$ or 0.5). (c) Dependence of the luminescence intensities of red emission from Mn⁴⁺ and blue emission from Bi³⁺ on Mn⁴⁺ doping concentrations. (d) The proposed energy level diagram scheme for the CAZO:Bi³⁺,Mn⁴⁺ phosphor and the energy transfer process.



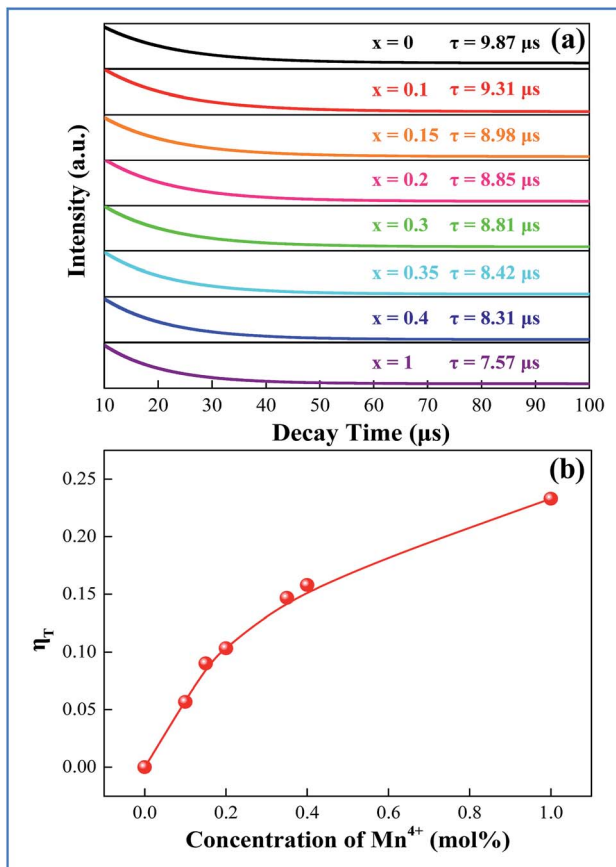


Fig. 5 (a) Decay curves (monitored at 410 nm and excited at 346 nm) of Bi^{3+} in the CAZO:0.5% $\text{Bi}^{3+}, x\% \text{Mn}^{4+}$ ($x = 0.05\text{--}0.5$) phosphors. (b) The efficiency of energy transfer from Bi^{3+} to Mn^{4+} as a function of Mn^{4+} concentration.

On the basis of Dexter's energy transfer formula of multipolar interactions, the following relationship can be given:²⁷⁻²⁹

$$\frac{\eta_0}{\eta_s} \propto C_{\text{Bi}^{3+} + \text{Mn}^{4+}}^{3/n} \quad (5)$$

where η_0/η_s is the ratio of the quantum efficiencies of Bi^{3+} in the absence and presence of Mn^{4+} , C is the sum concentration of Bi^{3+} and Mn^{4+} and n is a constant which can indicate the interaction between Bi^{3+} and Mn^{4+} , where $n = 6, 8$ and 10 , corresponding to dipole-dipole, dipole-quadrupole and quadrupole-quadrupole interactions, respectively. The value of η_0/η_s can be approximately calculated from the ratio of the related luminescence intensities (I_0/I_s) according to formulas (5) and (6):²⁷⁻²⁹

$$\frac{I_0}{I_s} \propto C_{\text{Bi}^{3+} + \text{Mn}^{4+}}^{3/n} \quad (6)$$

where I_0 and I_s are the intrinsic luminescence intensities of Bi^{3+} in the absence and presence of Mn^{4+} . Plots of the values of $\frac{I_0}{I_s}$ and $C_{\text{Bi}^{3+} + \text{Mn}^{4+}}^{n/3}$ ($n = 6, 8$ or 10) are shown in Fig. 6. It could be easily observed that a good linear behavior occurs only when $n = 6$; it shows a best linear relation with goodness of fit of $R^2 = 0.9911$, implying that the energy transfer from Bi^{3+} to Mn^{4+} occurs predominantly *via* a dipole-dipole interaction mechanism.

3.4 Improvement of the total internal QY of the phosphor due to the energy transfer from Bi^{3+} to Mn^{4+} ions

The QY is a key parameter to evaluate a luminescence material. It is defined as the ratio of emitted photons to absorbed ones. As shown in Fig. 7, the excitation lines and emission spectra of CAZO: Bi^{3+} , CAZO: Mn^{4+} and CAZO: $\text{Bi}^{3+}, \text{Mn}^{4+}$ were measured using an integrating sphere coated with BaSO_4 . The absorbance of the phosphor was calculated according to the following eqn (7):^{22,30,31}

$$A = \frac{L_b - L_c}{L_b} \quad (7)$$

where L_b is the integrated excitation profile when the sample is diffusely illuminated by the integrated sphere's surface and L_c is the integrated excitation profile when the sample is directly excited by the incident beam. The QY Φ_f of the sample was calculated according to the following equation:³⁰

$$\Phi_f = \frac{E_c - (1 - A)E_b}{L_a A} \quad (8)$$

where E_c is the integrated luminescence of the sample caused by direct excitation and E_b is the integrated luminescence of the sample caused by indirect illumination from the sphere that can be set to zero because the secondary absorption and emission from the sample can be ignored in our case. The term L_a is the integrated excitation profile from an empty integrated sphere (without the sample) that is almost the same as L_b . As shown in Fig. 7, the calculated QYs of CAZO:0.5% Bi^{3+} , CAZO:0.5% Mn^{4+} and CAZO:0.1% $\text{Bi}^{3+}, 0.5\% \text{Mn}^{4+}$ are 49.0%, 19.4%, and 89.1%, respectively.

In order to explain the phenomenon that the QY of CAZO: $\text{Bi}^{3+}, \text{Mn}^{4+}$ is much higher than any of the Bi^{3+} or Mn^{4+} singly doped samples, a series of samples CAZO: $x\% \text{Bi}^{3+}, 0.5\% \text{Mn}^{4+}$ ($x = 0.05, 0.1, 0.5, 1, 2, 3, 4$ or 5) were investigated and their emission spectra under excitation at 351 nm are shown in Fig. 8. The total luminescence intensities from both Bi^{3+} and Mn^{4+} are varying with the concentration of Bi^{3+} ion as shown in Fig. 4c and the insert of Fig. 8. To obtain the highest luminescence

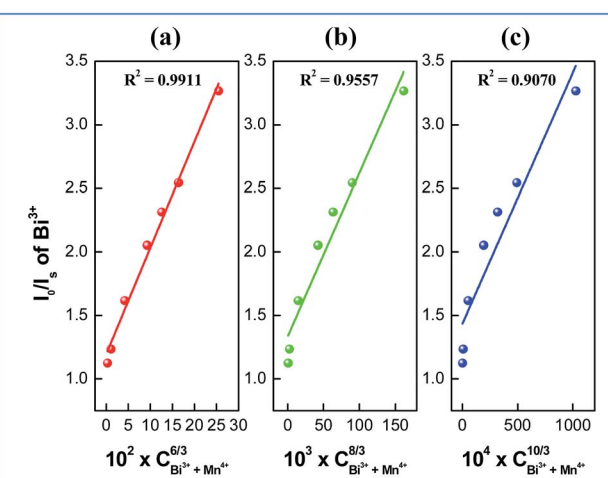


Fig. 6 Dependence of I_0/I_s of Bi^{3+} on (a) $C^{6/3}$, (b) $C^{8/3}$ and (c) $C^{10/3}$.

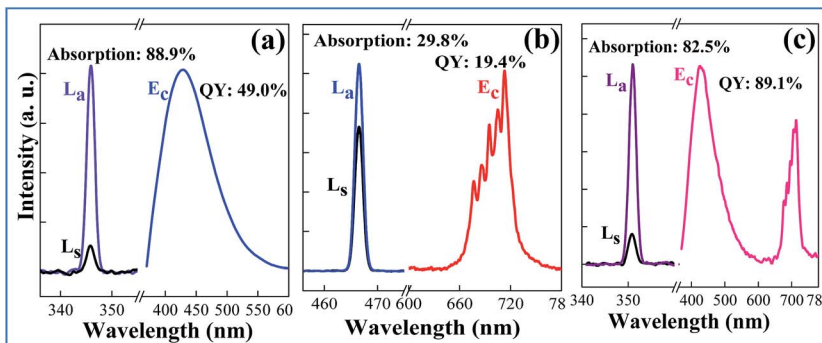


Fig. 7 The excitation lines and emission spectra of the as-prepared samples (a) CAZO:0.5% Bi^{3+} , (b) CAZO:0.5% Mn^{4+} , and (c) CAZO:1% Bi^{3+} , 0.5% Mn^{4+} for measurement of the quantum yield using an integrating sphere.

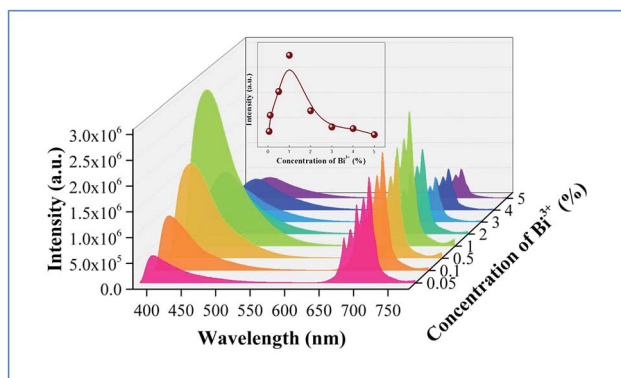


Fig. 8 Emission ($\lambda_{\text{ex}} = 351$ nm) spectra of typical samples of CAZO:x% Bi^{3+} , 0.5% Mn^{4+} ($x = 0.05, 0.1, 0.5, 1, 2, 3, 4$ or 5). Insert: the total luminescence intensities from both Bi^{3+} and Mn^{4+} varied with the concentration of Bi^{3+} ions.

intensity, the optimum concentration of Bi^{3+} in CAZO: Bi^{3+} is 0.5 mol% (Fig. 3b) while that in CAZO: $\text{Bi}^{3+}, \text{Mn}^{4+}$ is 1.0 mol%, which signifies the increased concentration of luminescence centers in Bi^{3+} and Mn^{4+} co-doped samples. The doping concentration of Bi^{3+} is increased by two times due to the energy transfer from Bi^{3+} to Mn^{4+} and decreased non-radiative transitions between the Bi^{3+} donors.⁷ Thus, the total internal QY of the Bi^{3+} and Mn^{4+} co-doped phosphor is increased obviously by the increased radiative emissions from both Bi^{3+} and Mn^{4+} .

4. Conclusion

In summary, a novel blue-emitting phosphor CAZO: Bi^{3+} was prepared using a solid state method. The phosphor CAZO: Bi^{3+} exhibits a broad blue emission peak with a maximum at 467 nm that originates from the ${}^3\text{P}_1 - {}^1\text{S}_0$ transition of Bi^{3+} . The emission intensities and lifetime values of the Bi^{3+} emission of the phosphors CAZO: $\text{Bi}^{3+}, \text{Mn}^{4+}$ decrease linearly with increasing concentration of Mn^{4+} , which strongly verified that an effective energy transfer occurred from Bi^{3+} to Mn^{4+} in the CAZO host. The efficiency of energy transfer between Bi^{3+} and Mn^{4+} is about 23.7%. The internal QY of CAZO: $\text{Bi}^{3+}, \text{Mn}^{4+}$ is as high as 89.1% due to increasing of the optimum concentration of Bi^{3+} ions.

The as-synthesized color-tunable phosphors have potential applications in NUV white LEDs in agricultural industry.

Acknowledgements

This research was jointly supported by the National Natural Science Foundation of China (51572200, 51102185, U1301242) and Zhejiang Province (Y16E020041), Public Industrial Technology Research Projects of Zhejiang Province (2015C31142), Research Fund for the Doctoral Program of Higher Education of China (20130171130001), and Key Laboratory of Optoelectronic Materials Chemistry and Physics, Chinese Academy of Sciences (2008DP173016).

References

- 1 G. Tamulaitis, P. Duchovskis, Z. Bliznikas, K. Breivé, R. linskaité, A. Brazaityté, A. Novičkovas and A. Žukauskas, *J. Phys. D: Appl. Phys.*, 2005, **38**, 3182–3187.
- 2 L. Ma, D. J. Wang, Z. Y. Mao, Q. F. Lu and Z. H. Yuan, *Appl. Phys. Lett.*, 2008, **93**, 144101.
- 3 N. Yeh and J. P. Chung, *Renewable Sustainable Energy Rev.*, 2009, **13**, 2175–2180.
- 4 J. Y. Chen, N. M. Zhang, C. F. Guo, F. J. Pan, X. J. Zhou, H. Suo, X. Q. Zhao and E. M. Goldys, *ACS Appl. Mater. Interfaces*, 2016, **8**, 20856–20864.
- 5 F. W. Kang, M. Y. Peng, D. Y. Lei and Q. Y. Zhang, *Chem. Mater.*, 2016, **28**, 7807–7815.
- 6 F. W. Kang, H. S. Zhang, L. Wondraczek, X. B. Yang, Y. Zhang, D. Y. Lei and M. Y. Peng, *Chem. Mater.*, 2016, **28**, 2692–2703.
- 7 L. L. Wang, Q. L. Wang, X. Y. Xu, J. Z. Li, L. B. Gao, W. K. Kang, J. S. Shi and J. Wang, *J. Mater. Chem. C*, 2013, **1**, 8033–8040.
- 8 R. V. Yadav, R. S. Yadav, A. Bahadur, A. K. Singh and S. B. Rai, *Inorg. Chem.*, 2016, **55**, 10928–10935.
- 9 H. Y. Tan, M. Z. Rong, Y. Y. Zhou, Z. Y. Yang, Z. L. Wang, Q. H. Zhang, Q. Wang and Q. Zhou, *Dalton Trans.*, 2016, **45**, 9654–9660.
- 10 Y. W. Zhu, L. Huang, R. Zou, J. H. Zhang, J. B. Yu, M. M. Wu, J. Wang and Q. Su, *J. Mater. Chem. C*, 2016, **4**, 5690–5695.



11 D. Sekiguchi and S. Adachi, *ECS J. Solid State Sci. Technol.*, 2014, **3**, R60–R64.

12 S. P. Singh, M. Kim, W. B. Park, J. W. Lee and K. S. Sohn, *Inorg. Chem.*, 2016, **55**, 10310–10319.

13 X. Ding, G. Zhu, W. Y. Geng, Q. Wang and Y. H. Wang, *Inorg. Chem.*, 2016, **55**, 154–162.

14 B. Wang, H. Lin, F. Huang, J. Xu, H. Chen, Z. B. Lin and Y. S. Wang, *Chem. Mater.*, 2016, **28**, 3515–3524.

15 R. P. Cao, M. Y. Peng, E. H. Song and J. R. Qiu, *ECS J. Solid State Sci. Technol.*, 2012, **1**, R123–R126.

16 W. Lü, W. Z. Lv, Q. Zhao, M. M. Jiao, B. Q. Shao and H. P. You, *Inorg. Chem.*, 2014, **53**, 11985–11990.

17 T. Hasegawa, S. W. Kim, T. Abe, S. Kumagai, R. Yamanashi, K. Seki, K. Uematsu, K. Toda and M. Sato, *Chem. Lett.*, 2016, **45**, 1096–1098.

18 W. Lü, M. M. Jiao, B. Q. Shao, L. F. Zhao, Y. Feng and H. P. You, *Dalton Trans.*, 2016, **45**, 466–468.

19 J. H. Chen, W. R. Zhao, N. H. Wang, Y. J. Meng, S. P. Yi, J. He and X. Zhang, *J. Mater. Sci.*, 2016, **51**, 4201–4212.

20 X. J. Gao, W. Li, X. L. Yang, X. L. Jin and S. G. Xiao, *J. Phys. Chem. C*, 2015, **119**, 28090–28098.

21 G. Blasse and A. Bril, *J. Chem. Phys.*, 1968, **48**, 217–222.

22 W. Chao, P. L. Li, Z. J. Wang, Y. S. Sun, J. G. Cheng, Z. L. Li, M. M. Tian and Z. P. Yang, *Phys. Chem. Chem. Phys.*, 2016, **18**, 28661–28673.

23 S. H. Miao, Z. G. Xia, J. Zhang and Q. L. Liu, *Inorg. Chem.*, 2014, **53**, 10386–10393.

24 E. Cavalli, F. Angiuli, F. Mezzadri, M. Trevisani, M. Bettinelli, P. Boutinaud and M. G. Brik, *J. Phys.: Condens. Matter*, 2014, **26**, 385503.

25 R. J. Xie, N. Hirosaki, T. Suehiro, F. F. Xu and M. Mitomo, *Chem. Mater.*, 2006, **18**, 5578–5583.

26 B. M. Antipeuko, I. M. Bataev, V. L. Ermolaev and T. A. Privalova, *Opt. Spectrosc.*, 1970, **29**, 335.

27 G. Blasse, Energy Transfer in Oxidic Phosphors, *Philips Res. Rep.*, 1969, **24**, 131–144.

28 R. Reisfeld, E. Greenberg, R. Velapoldi and B. Barnett, *J. Chem. Phys.*, 1972, **56**, 1698–1705.

29 D. L. Dexter and J. H. Schulman, *J. Chem. Phys.*, 1954, **22**, 1063–1070.

30 *Integrating Sphere F-3018 Operation Manual Part number 81089 version 1.1*, provided by HORIBA Jobin Yvon Inc., May, 2005.

31 B. Wang, H. Lin, J. Xu, H. Chen and Y. S. Wang, *ACS Appl. Mater. Interfaces*, 2014, **6**, 22905–22913.

